# Influences of an Entrainment-Mixing Parameterization on Numerical Simulations of Cumulus and Stratocumulus Clouds

Xiaoqi Xu[1,2,4], Chunsong Lu[1*], Yangang Liu[3*], Shi Luo[1,5], Xin Zhou[3], Satoshi Endo[3], Lei Zhu[1], Yuan Wang[1]

1. Key Laboratory for Aerosol-Cloud-Precipitation of China Meteorological Administration/Collaborative Innovation Center on Forecast and Evaluation of Meteorological Disasters (CIC-FEMD), Nanjing University of Information Science & Technology, Nanjing, China

2. Nanjing Joint Institute for Atmospheric Sciences, Nanjing, China

3. Environmental and Climate Sciences Department, Brookhaven National Laboratory, Upton, US

4. Key Laboratory of Transportation Meteorology, CMA, Nanjing, China

5. College of Aviation Meteorology, Civil Aviation Flight University of China, Guanghan, China

* Correspondence: luchunsong110@gmail.com; lyg@bnl.gov

**Abstract**

Different entrainment-mixing processes can occur in clouds; however, a homogeneous mixing mechanism is often implicitly assumed in most commonly used microphysics schemes. Here, we first present a new entrainment-mixing parameterization that uses the grid-mean relative humidity without requiring the relative humidity of the entrained air. Then, the parameterization is implemented in a microphysics scheme in a large eddy simulation model, and sensitivity experiments are conducted to compare the new parameterization with the default homogeneous entrainment-mixing parameterization. The results indicate that the new entrainment-mixing parameterization has a larger impact on the number concentration, volume-mean radius, and cloud optical depth in the stratocumulus case than in the cumulus case. This is because inhomogeneous and homogeneous mixing mechanisms dominate in the stratocumulus and cumulus cases, respectively, which is mainly due to the larger turbulence dissipation rate in the cumulus case. Because stratocumulus clouds break up during the dissipation stage to form cumulus clouds, the effects of this new entrainment-mixing parameterization during the stratocumulus dissipation stage are between those during the stratocumulus mature stage and the cumulus case. A large aerosol concentration can enhance the effects of this new entrainment-mixing parameterization by decreasing the cloud droplet size and evaporation time scale. The results of this new entrainment-mixing parameterization with grid-mean relative humidity are validated by use of a different entrainment-mixing parameterization that uses parameterized

38  entrained air properties. This study sheds new light on the improvement of entrainment-

39  mixing parameterizations in models.

## 1. Introduction

42      The process of entrainment and subsequent mixing between clouds and their

43  environment is one of the most uncertain processes in cloud physics, which is thought

44  to be crucial to many outstanding issues, including warm-rain initiation and subsequent

45  precipitation characteristics, cloud-climate feedback, and evaluating the indirect effects

46  of aerosol (Paluch and Baumgardner, 1989; Yum, 1998; Ackerman et al., 2004; Kim et

47  al., 2008; Huang et al., 2008; Del Genio and Wu, 2010; Lu et al., 2011; Lu et al., 2014;

48  Kumar et al., 2013; Zheng and Rosenfeld, 2015; Fan et al., 2016; Gao et al., 2020; Gao

49  et al., 2021; Zhu et al., 2021; Xu et al., 2021; Kumar et al., 2013; Yang et al., 2016;

50  Yang et al., 2021). The most well-studied concepts are homogeneous/inhomogeneous

51  entrainment-mixing mechanisms. During homogeneous mixing, all droplets experience

52  evaporation, and no droplet is evaporated completely. During extremely

53  inhomogeneous mixing, some droplets near the entrained air evaporate completely,

54  while the remaining droplets maintain their original sizes. If the situation is somewhere

55  between these two extreme scenarios, an inhomogeneous mixing process occurs. Some

56  studies suggest that homogeneous mixing is likely to be typical (Jensen et al., 1985;

57  Burnet and Brenguier, 2007; Lehmann et al., 2009), whereas others have claimed that

58  extremely inhomogeneous scenario is dominant (Pawlowska et al., 2000; Burnet and

59    Brenguier, 2007; Haman et al., 2007; Freud et al., 2008; Freud et al., 2011). Different

60    mechanisms can be undistinguishable when the relative humidity in the entrained air is

61    high (Gerber et al., 2008).

62    Some sensitivity studies assuming homogeneous or extremely inhomogeneous

63    mixing have found that different mixing mechanisms can significantly influence the

64    microphysics and radiative properties of clouds (Lasher-Trapp et al., 2005; Grabowski,

65    2006; Chosson et al., 2007; Slawinska et al., 2008). For example, Grabowski (2006)

66    used a cloud-resolving model and found that the amount of solar energy reaching the

67    surface in the pristine case, assuming the homogeneous mixing scenario, is the same as

68    in the polluted case with extremely inhomogeneous mixing. This result was verified by

69    Slawinska et al. (2008) using a large-eddy simulation (LES) model. Although the

70    influence of different mixing mechanisms in simulations is lower when two-moment

71    microphysics schemes are used (Hill et al., 2009; Grabowski and Morrison, 2011;

72    Slawinska et al., 2012; Xu et al., 2020), Hill et al. (2009) also claimed that there are

73    still many uncertainties in the entrainment-mixing process, and the effect of different

74    mixing mechanisms can be more important over the entire cloud life-cycle.

75    In recent years, methods have been developed to describe general entrainment-

76    mixing processes, with homogeneous and extremely inhomogeneous scenarios as

77    special cases (Andrejczuk et al., 2006; Andrejczuk et al., 2009; Lehmann et al., 2009;

78    Lu et al., 2011). Hoffmann et al. (2019) and Hoffmann and Feingold (2019) conducted

79    LES at the subgrid-scale with turbulent mixing, using a linear eddy model. Andrejczuk

80   et al. (2009) used the results of direct numerical simulation (DNS) to establish a

81   relationship between instantaneous microphysical properties and Damköhler number

82   ($D_a$, Burnet and Brenguier, 2007), and developed a parameterization of the entrainment-

83   mixing process. Lu et al. (2013) developed a parameterization of the entrainment-

84   mixing process based on the relationship between the homogeneous mixing degree ($\psi$)

85   and transition scale number ($N_L$) in the explicit mixing parcel model (EMPM), as well

86   as aircraft observation data. Gao et al. (2018) investigated how $\psi$ is related to $D_a$ and

87   $N_L$ in a DNS, to improve the parameterization of the entrainment-mixing process. Luo

88   et al. (2020) simulated more than 12,000 cases with EMPM by changing a variety of

89   parameters affecting entrainment-mixing processes and developed a parameterization

90   that improved the one proposed by Lu et al. (2013).

91       Although several entrainment-mixing parametrizations have been proposed, to the

92   best of our knowledge, only one study (Jarecka et al., 2013) has coupled an entrainment-

93   mixing parameterization with cloud microphysics to consider the change in cloud

94   droplet concentration during the entrainment-mixing process. Jarecka et al. (2013)

95   applied an entrainment-mixing parameterization, in terms of the Damköhler number, to

96   a two-moment microphysics scheme and found small impacts of entrainment-mixing

97   parameterization in shallow cumulus clouds. To further explore the influences of

98   entrainment-mixing processes, this study first modifies the entrainment-mixing

99   parameterization in terms of the transition scale number proposed by Luo et al. (2020)

100  to couple it more easily with microphysics schemes. The parameterization is then

101 implemented in the two-moment Thompson aerosol-aware scheme (Thompson and

102 Eidhammer, 2014). Finally, the effects of parameterization on the physical properties

103 of clouds are examined in both cumulus and stratocumulus clouds.

104     The rest of this paper is organized as follows: Section 2 describes the new

105 entrainment-mixing parameterization, simulated cases, and modelling setup. The major

106 results are presented and discussed in Section 3. The influences of the new entrainment-

107 mixing parameterization on cloud physics and the underlying mechanisms are

108 examined, and the effects of turbulence dissipation rate ($\varepsilon$) and aerosol concentration

109 are also discussed. Some concluding remarks are presented in Section 4.

110

**111 2. Parameterization, simulated cases, and modeling setup**

**112 2.1 The new entrainment-mixing parameterization**

113     According to Morrison and Grabowski (2008), the effect of the entrainment-

114 mixing process on cloud microphysical properties can be expressed as follows:

$$115 \qquad N_\mathrm{c} = N_\mathrm{c0}\left(\frac{q_\mathrm{c}}{q_\mathrm{c0}}\right)^{\alpha}, \qquad (1)$$

116 where $N_\mathrm{c}$ and $N_\mathrm{c0}$ are the cloud droplet number concentrations after and before the

117 evaporation process, respectively, and $q_\mathrm{c}$ and $q_\mathrm{c0}$ represent the corresponding cloud

118 water mixing ratios. It is noteworthy that when a new saturation is achieved after

119 evaporation, $q_\mathrm{c}$ is determined by $q_\mathrm{c0}$, relative humidity (RH), air pressure, and

120 temperature. The parameter $\alpha$ can be pre-set to any value between 0 (homogeneous

121 mixing) and 1 (extremely inhomogeneous mixing) to represent a different degree of

122 subgrid-scale mixing homogeneity. In this study, instead of specifying $\alpha$ as a

123 predetermined constant, here it is determined through expressions (Lu et al., 2013; Luo

124 et al., 2020)

$$\alpha = 1 - \psi, \tag{2a}$$

$$\psi = c \exp(a N_{\mathrm{L}}^{b}). \tag{2b}$$

127 where $a$, $b$ and $c$ are the three fitting parameters (Luo et al., 2020). The dimensionless

128 number $N_{\mathrm{L}}$ is a dynamical measure of the degree of subgrid-scale mixing homogeneity

129 (Lu et al., 2011) defined by

$$N_{\mathrm{L}} = \frac{L^*}{\eta}, \tag{3a}$$

$$\eta = \left( v^3 / \varepsilon \right)^{1/4}, \tag{3b}$$

$$L^* = \varepsilon^{1/2} \tau_{\mathrm{evap}}^{3/2}, \tag{3c}$$

133 where $L^*$ is the transition length (Lehmann et al., 2009), $\eta$ is the Kolmogorov microscale,

134 $v$ is the kinematic viscosity; $\varepsilon$ is calculated from the subgrid turbulent kinetic energy

135 (Deardorff, 1980):

$$\varepsilon = C E^{3/2} / L, \tag{4}$$

137 where $C = 0.70$ is an empirical constant, $E$ is the subgrid turbulent kinetic energy, and

138 $L$ is the model grid size.  The evaporation time scale ($\tau_{\mathrm{evap}}$) is defined as the time taken

139 for droplets to evaporate completely in an unsaturated environment, and is calculated

140 as

$$\tau_{\mathrm{evap}} = -\frac{r^2}{2 A S_{\mathrm{e}}}, \tag{5a}$$

142
$$A = \cfrac{1}{\left[\left(\cfrac{L_h}{R_v T} - 1\right)\cfrac{L_h \rho_L}{KT} + \cfrac{\rho_L R_v T}{D e_s(T)}\right]},$$
(5b)

where $r$ is the volume-mean radius of cloud droplets, $A$ is a function of pressure and

temperature, $S_e$ is the supersaturation (RH-1) of entrained air, $L_h$ is the latent heat, $R_v$ is

the specific gas constant for water vapour, $T$ is air temperature, $\rho_L$ is the density of liquid

water, $K$ is the coefficient of thermal conductivity of air, $D$ is the diffusion coefficient

of water vapour in the air, and $e_s(T)$ is the saturation vapour pressure over a plane water

surface at temperature $T$.

Unfortunately, $S_e$ in Equation (5a) is generally unavailable in atmospheric models,

including LES models. Thus, the entrainment-mixing parameterization developed by

Luo et al. (2020) based on the properties of entrained air cannot be used directly. To

solve this problem, we modify the entrainment-mixing parameterization of Luo et al.

(2020) by replacing $S_e$ with the domain-mean RH in the EMPM, after entrainment but

before evaporation, based on 12,218 cases:

$$\psi = 107.19 \exp(-1.99 N_L^{-0.29}).$$
(6)

Figure 1 shows the fitting results of the modified new entrainment-mixing

parameterization. Compared to the parametrization proposed by Luo et al. (2020), the

modified parameterization has similar $\psi$-$N_L$ distributions, but with a larger $N_L$ for the

same $\psi$, because the EMPM domain-mean RH is larger than the entrained air RH. With

this modification, $N_L$, $\psi$, and thus the effect of the entrainment-mixing processes on

droplet concentration can be directly calculated using the LES grid-mean RH. It is

162    important to note that the parameterization does not mean that the entrained air RH is

163    equal to that of the LES grid-mean RH. It is also worth noting that a wide range of $\varepsilon$,

164    $S_e$, and fraction of entrained air ($f$) are taken into account when establishing the

165    parameterization with the EMPM. The details of the EMPM simulations and related

166    calculations are provided by Luo et al. (2020).

167

168    **2.2 LES model, simulation cases, and modelling setup**

169        The LES model is built by applying the large-scale forcing module presented in

170    Endo et al. (2015) to the Weather Research and Forecasting (WRF) model tailored for

171    solar irradiance forecasting (WRF-Solar, Hacker et al., 2016; Haupt et al., 2016). The

172    large-scale forcing data (VARANAL) used in this process is derived from the

173    constrained variational analysis (CVA) approach developed by Zhang et al. (2001) and

174    provided by the U.S. Department of Energy's Atmospheric Radiation Measurement

175    Program (www.arm.gov). The modified entrainment-mixing parameterization is

176    implemented in the two-moment Thompson aerosol-aware scheme (Thompson and

177    Eidhammer, 2014).

178        To investigate the behaviours of the new entrainment-mixing parameterization in

179    different cloud types, cumulus and stratocumulus cases are simulated. For both the

180    cumulus and stratocumulus cases, the horizontal resolution of the model is 100 m × 100

181    m with a domain area of 14.4 km × 14.4 km. The vertical direction is divided into 225

182    layers with a resolution of 30 m.

183    For each cloud case, $\psi$ is first set to 1 for the *default* experiment because most LES

184    models assume a homogeneous entrainment-mixing mechanism. The simulation with

185    the new entrainment-mixing parameterization (Equations (1-6)) is hereafter referred to

186    as *new*. First, $N_L$ is diagnosed for each grid, and $\psi$ is then calculated using Equation (6).

187    Finally, the variation in $N_c$ during entrainment-mixing is obtained using Equations (1)

188    and (2a). To examine the influence of the aerosol number concentration on the

189    entrainment-mixing process, we conduct the numerical experiments *default_10* and

190    *new_10* by multiplying the initial aerosol number concentrations, for the *default* and

191    *new* models, respectively, by a factor of 10. Thus, four sets of numerical experiments

192    are conducted for both the cumulus and stratocumulus cases; the names of the

193    experiments and corresponding descriptions are summarized in Table 1.

194

195    **3. Results**

196    **3.1 Cumulus case**

197    For the cumulus case, the simulation starts at 12:00 UTC on 11 June 2016 and

198    ends at 03:00 UTC on 12 June 2016 with an output interval of 10 min and spin-times

199    of 3 h. To demonstrate the utility of the model, Figure 2 compares the temporal

200    evolution of the observed and simulated cloud fraction (a) and solar irradiance (b) from

201    the *default* experiment. Grid points with $q_c$ larger than 0.01 g/kg are defined as "cloudy

202    areas". Also shown for comparison is observational data with a one-hour temporal

203    resolution, which is provided by the LES Atmospheric Radiation Measurement

204   Symbiotic Simulation and Observation (LASSO) campaign (Gustafson et al., 2020).

205   The observations show that the cloud forms at 12:00 UTC on 11 June and dissipates

206   completely by 01:00 UTC on 12 June with a maximum cloud fraction of 0.47 at 16:00

207   UTC on 11 June. Considering the difference between the solar irradiances obtained

208   from point measurements and the value representing the simulation domain, the

209   observed solar irradiance at the Southern Great Plains (SGP) Central Facility are

210   compared with the results of central grid point in simulation (Figure 2(b)). Evidently,

211   although the results of simulation do not fluctuate as much as the observations, the

212   model captures the general behaviours of both cloud fraction and solar irradiance. The

213   general agreement between the simulations and observations lends credence to using

214   the model in further study.

215       Figure 3 shows the evolution of the microphysical and optical properties of clouds

216   in the cloudy areas of all simulation experiments, including $q_c$, $N_c$, droplet volume-

217   mean radius ($r_v$), cloud water path (CWP), and cloud optical depth ($\tau$). To visually and

218   simultaneously compare the change in cloud droplet concentration under different

219   aerosol concentrations, the maximum cloud droplet concentration ($N_{cmax}$) from *default*

220   is used to normalize $N_c$ in *default* and *new*, while $N_{cmax}$ from *new_10* is used to

221   normalize $N_c$ in *default_10* and *new_10*. The CWP is calculated as:

$$\mathrm{CWP} = \int_0^H \rho_a q_c(z)dz, \tag{7}$$

223   where $\rho_a$ is the air density, $q_c(z)$ is the cloud water mixing ratio at each height ($z$), and

224   *H* is the cloud thickness. The optical depth $\tau$ is estimated with

$$\tau = \frac{3}{2}\frac{1}{\rho_w}\int_0^H \frac{\rho_a q_c(z)}{r_e(z)}dz, \tag{8}$$

225

226 where $\rho_w$ is the water density and $r_e(z)$ is the effective radius of the cloud droplets at

227 each height ($z$). The time-averaged values of these physical properties of the clouds are

228 listed in Table 2 for convenience.

229     For the low aerosol number concentration, the simulations with the new

230 entrainment-mixing parameterization have smaller $N_c$ (35.53 cm$^{-3}$) and larger $r_v$ (13.29

231 μm) than the default homogeneous simulation (35.78 cm$^{-3}$ for $N_c$ and 13.27 μm for $r_v$

232 in *default*). However, comparing *new* to *default*, the relative changes in $N_c$, $r_v$, and $\tau$ are

233 very small. When the aerosol concentration increases ten-fold (*default_10* and *new_10*),

234 $q_c$, CWP, and $\tau$ increase according to the aerosol indirect effect (Peng et al., 2002; Wang

235 et al., 2019; Li et al., 2011; Wang et al., 2011). Meanwhile, $r_v$ decreases significantly

236 owing to the larger cloud number concentration. The effects of the new entrainment-

237 mixing parameterization also increase, for example, the change in $N_c$ increases from –

238 0.70% (*new* compared to *default*) to –2.74% (*new_10* compared to *default_10*), $r_v$

239 increases from +0.15% to +0.57%, and $\tau$ from –0.38% to –0.58%; the reasons for these

240 changes are discussed later. These small changes are similar to those identified in

241 previous cumulus studies (Jarecka et al., 2013; Hoffmann et al., 2019).

242

243 **3.2 Stratocumulus case**

244     The stratocumulus case is simulated from 9:00 UTC on 19 April 2009 to 03:00

245 UTC on 20 April 2009; the first three hours are set to be spin-up times. We examine the

246     stratocumulus region of the cloud base at ~2.1 km and the cloud top at ~2.3 km (cloud

247     thickness of ~200 m). Figure 4 shows the time series of the domain-averaged cloud

248     fraction and total downward irradiance at the central point in the observation and the

249     *default* experiment from 12:00 UTC to 24:00 UTC. Similar to the cumulus case, the

250     simulations compare favourably with the observations, which further reinforces the

251     utility of the LES model. The observed data show that the cloud fraction increases with

252     time and peaks at 16:00 UTC. The simulated cloud fraction has a value of 1 before

253     16:00 UTC, fluctuates from 16:00 UTC to 21:00 UTC, and decreases sharply after

254     21:00 UTC. This period can be divided into three stages, namely the mature stage, pre-

255     dissipation stage, and dissipation stage.

256     As with the cumulus case, the temporal evolutions of the physical properties ($q_c$,

257     $N_c$, $r_v$, CWP, and $\tau$) of the clouds are shown in Figure 5. In contrast to the oscillating

258     changes exhibited by the physical quantities in the cumulus case (Figure 3), the physical

259     properties in the stratocumulus case exhibit a mostly smooth temporal evolution.

260     Furthermore, *default* and *new* exhibit clear distinctions during the early periods, but

261     these differences decrease during the dissipation stage. This is also the case with

262     *default_10* and *new_10*.

263     To compare the different behaviours of the simulation experiments at different

264     stages, the results at the mature and dissipation stages are analysed in detail. The mean

265     values of the main microphysical and optical properties of the clouds are summarised

266     in Table 3. As expected, the cloud microphysical and optical properties at the mature

267   stage are all larger than those at the dissipation stage. The effects of the new

268   entrainment-mixing parametrization are also more significant at the mature stage.

269   Compared to *default*, the *new* model results in a 7.36% smaller $N_c$, 3.20% larger $r_v$, and

270   5.98% smaller $\tau$ during the mature stage. During the dissipation stage, the changes in

271   $N_c$, $r_v$, and $\tau$ are –4.76%, +2.12 %, and –2.56%, respectively. The largest influence of

272   the new entrainment-mixing parametrization occurs during the mature stage when the

273   aerosol concentration is ten times greater. The differences in $N_c$, $r_v$, and $\tau$ between

274   *new_10* and *default_10* are –9.69%, +3.88%, and –5.85%, respectively, averaged over

275   the mature stage. These differences are much larger than those reported by Hill et al.

276   (2009) who found that assuming extremely inhomogeneous mixing has a negligible

277   effect on stratocumulus simulations. Our results also prove the speculation of Hill et al.

278   (2009) that the mixing process might play an important role when the stratocumulus is

279   thin (~200 m in this study). Furthermore, implementing the new entrainment-mixing

280   parameterization has similar effects on cloud properties to those described by Hoffmann

281   and Feingold (2019) who used the linear eddy model to represent subgrid-scale

282   turbulent mixing. Note that stratocumulus clouds occur in most regions around the

283   world and are important contributors to the surface radiation budget (Wood, 2012;

284   Zheng et al., 2016; Wang et al., 2021; Wang and Feingold, 2009). Stratocumulus clouds

285   dominate in some regions and occur over 60% of the time as vast long-lived sheets,

286   such as the *semi-permanent subtropical marine stratocumulus sheets* (Wood, 2012). In

287   these regions, a nearly 6% decrease in $\tau$, caused by the new entrainment-mixing

288    parameterization is expected to have significant effects on the simulation of regional

289    radiative properties and climate change.

290        The averaged influences of the new entrainment-mixing parametrization over all

291    the simulation periods are also examined (Table 4). Quantitatively, the effect of the new

292    entrainment-mixing parameterization is much greater on stratocumulus clouds than on

293    cumulus clouds. Compared to *default*, *new* has an average change of –6.20% in $N_c$,

294    +2.01% in $r_v$, and –3.23% in $\tau$. When the aerosol concentration increases ten-fold, the

295    differences in $N_c$, $r_v$, and $\tau$ between *default_10* and *new_10* are −9.00%, +3.16%, and

296    −4.14%, respectively. These differences are larger than the largest changes in the

297    cumulus case.

298

299    **3.3 Mechanisms of the effects of the new entrainment-mixing parameterization**

300        The different effects of the new entrainment-mixing parameterization on different

301    types of clouds and even on different stages of stratocumulus clouds are likely be related

302    to variations in the dominant mixing mechanism. To confirm this, we calculate the

303    average $\psi$ at all grid points experiencing evaporation, the proportion of inhomogeneous

304    mixing grid points to all grid points experiencing evaporation, and the average $\psi$ at the

305    inhomogeneous mixing grid points in *new* and *new_10* (Table 5) for the cumulus case,

306    and mature and dissipation stages in the stratocumulus case.

307        For the cumulus case, simulations exhibit large $\psi$ and a small proportion of

308    inhomogeneous mixing, indicating that homogeneous mixing is the dominant

309   entrainment-mixing mechanism (Luo et al., 2020; Lu et al., 2013). Correspondingly,

310   the influences of the new entrainment-mixing parameterization on the cloud physical

311   properties are not significant, as shown in Figure 3 and Table 2. The *new_10* model

312   exhibit a smaller average $\psi$ and a larger proportion of inhomogeneous mixing than *new*,

313   which results in larger changes in cloud physics, as mentioned in Section 3.1.

314       For the stratocumulus case, Table 5 shows the average $\psi$ at all grid points

315   experiencing evaporation, the proportion of inhomogeneous mixing grid points to all

316   grid points experiencing evaporation, and the average $\psi$ at the inhomogeneous mixing

317   grid points during the two stages. The mature stage always has a smaller $\psi$ but a larger

318   proportion of inhomogeneous mixing than the dissipation stage. The inhomogeneous

319   mixing process dominates the mature stage in *new*, because more than 60% of the grid

320   points experience inhomogeneous mixing. The inhomogeneous mixing process is more

321   dominant in *new_10*, because less than 3% of the cloudy grid points experience a

322   homogeneous mixing process during the mature stage, which explains why *new_10* has

323   the largest influence when implementing the new entrainment-mixing parametrization.

324   Meanwhile, the average $\psi$ in both stages is smaller than that in the cumulus case for the

325   same simulation configuration. Thus, the effects of the new entrainment-mixing

326   parameterization are more significant for stratocumulus than for cumulus clouds,

327   especially at the mature stage. It is noted that the average $\psi$ and the proportion of

328   inhomogeneous mixing at the dissipation stage of *new* in the stratocumulus case are

329   very close to the results of *new_10* in the cumulus case. This is because the cloud

330    fraction decreases sharply during the dissipation stage; the stratocumulus clouds break

331    up and produces cumulus clouds with small cloud droplet radius.

332

333    **3.4 The effects of dissipation rate and aerosol concentration on the entrainment-**

334    **mixing process**

335        Previous studies have shown the notable effects of the dissipation rate and aerosol

336    concentration on the entrainment-mixing process. For example, Luo et al. (2020)

337    changed $\varepsilon$ from $10^{-5}$ m$^2$ s$^{-3}$ to $10^{-2}$ m$^2$ s$^{-3}$ and noted huge differences in the corresponding

338    $\psi$. Small et al. (2013) compared aircraft observations with different background

339    concentrations and found that higher pollution flights tended to slightly more

340    inhomogeneous mixing; Jarecka et al. (2013) also showed various homogeneities of

341    subgrid mixing when aerosol concentration increases ten-fold. To explain the different

342    behaviours of different simulations with the new entrainment-mixing parameterization,

343    the influences of $\varepsilon$ and aerosol concentration are examined. Figure 6 shows the

344    probability distribution functions (PDFs) of $\varepsilon$, $r_v$, $\tau_{evap}$, and $N_L$ for cloud grids

345    experiencing entrainment-mixing processes in *new* and *new_10* for the cumulus and

346    stratocumulus cases, respectively. The PDFs from the mature and dissipation stages of

347    the stratocumulus case are shown in Figure 7.

348

349    **3.4.1 Dissipation rate**

350        According to Equation (3), $N_L$ is a function of $\varepsilon^{3/4}$; hence, the PDF of $\varepsilon$ directly

351 affects $N_L$ and further results in different $\psi$. For the cumulus case, the mean $\varepsilon$ of 0.0043

352 m$^2$ s$^{-3}$ in *new* is similar to those obtained for cumulus clouds in previous studies (e.g.

353 Lu et al., 2016; Hoffmann et al., 2019). As shown in Figure 1, cloud grids experience a

354 homogeneous mixing process if $N_L$ is larger than $\sim 10^5$, the limited distribution of $N_L$

355 values less than $10^5$ in *new* results in a very small number of cloud grid points

356 undergoing inhomogeneous mixing process. Even at the cloud grid points that undergo

357 inhomogeneous mixing, the average $\psi$ is large (98.62%), because most of the $N_L$ values

358 are larger than $10^3$. Therefore, the cloud properties in *new* are close to those in *default*.

359    For the stratocumulus case, the mean value of $\varepsilon$ ($2.9 \times 10^{-4}$ m$^2$ s$^{-3}$ in *new*) is an order

360 of magnitude less than those in the cumulus case. Therefore, compared with the

361 cumulus case, $N_L$ is reduced in the stratocumulus case, while the peak value of *new*

362 almost reaches the criterion of inhomogeneous mixing ($\sim 10^5$). For the two stages of

363 stratocumulus clouds, $\varepsilon$ is an order of magnitude smaller, but $r_v$ was larger (Figure 7)

364 during the mature stage than during the dissipation stage. According to Equation (5a),

365 droplets with smaller $r_v$ are more prone to complete evaporation and have a smaller $\tau_{evap}$.

366 The combination of smaller $\varepsilon$ and larger $r_v$ results in a smaller $N_L$ (Equation (3)). This

367 is the reason for the new entrainment-mixing parametrization having more significant

368 effects during the mature stage than during the dissipation stage. In addition, the

369 similarity of the $\varepsilon$ and $r_v$ values during the dissipation stage of the stratocumulus case

370 in *new*, compared to the cumulus case in *new_10* (Figures 6a and 6b), explains the

371 similar average $\psi$ values of these scenarios and the proportion of inhomogeneous

372    mixing (Table 5).

373    Therefore, the distribution of $\varepsilon$ has a vital impact on the influence of the new

374    entrainment-mixing parameterization. Smaller values of $\varepsilon$ result in the new

375    entrainment-mixing parameterization having a more significant influence. Moreover,

376    the $r_v$ in the stratocumulus case is smaller than that in the cumulus case, which is also

377    conducive to a more inhomogeneous mixing process. These are the reasons why the

378    implementation of the new entrainment-mixing parameterization has a larger influence

379    in the stratocumulus case than in the cumulus case, when compared to a homogeneous

380    mixing mechanism.

381

382    **3.4.2 Aerosol concentration**

383    The aerosol concentration affects the entrainment-mixing process by decreasing

384    the cloud droplet radius. As $r_v$ decreases, the distributions of $\tau_{evap}$ in *new_10* moves to

385    a smaller overall value, while the mean value is an order of magnitude smaller than that

386    in *new*, which causes a much smaller $N_L$ because $N_L$ is proportional to $\tau_{evap}^{3/2}$ (Equations

387    (3a) and (3b)). The larger percentage of smaller $N_L$ values indicates that in *new_10*,

388    more grid points undergo an inhomogeneous mixing process, and the proportion of such

389    grid points is much larger than in the *new* model (Table 5). Therefore, compared to *new*,

390    *new_10* exhibit a smaller $\psi$ and the effects of the new entrainment-mixing

391    parameterization on cloud properties are more obvious, for both the cumulus and

392    stratocumulus cases.

393

## 3.5 Verification by the simulations with a different parameterization using entrained air relative humidity

In the above simulations, the new entrainment-mixing parameterization is based on the grid-mean RH. This section serves to verify these simulations using the the entrainment-mixing parameterization proposed by Luo et al. (2020)

$$\psi = 107.96 \exp(-0.95 N_{\text{L}}^{-0.35}), \tag{9}$$

which was developed using the entrained air RH in the EMPM. This parameterization needs the entrained air RH within each grid in WRF, which is estimated following Grabowski (2007) and Jarecka et al. (2009). Briefly, assuming that RH mixes linearly when the dry air entrains into the cloud, then entrained air RH can be simply calculated by

$$RH_{\text{entrained}} = \frac{RH_{\text{grid}} - (1-f)RH_{\text{cloud}}}{f}, \tag{10}$$

where the subscripts *entrained*, *cloud*, and *grid* indicate the RH of the entrained, cloudy, and grid point air, respectively. In Equation (10), although the cloudy air RH is approximately 100% and grid-mean RH is predicted in the model, the entrained air fraction $f$ needs to be further parameterized. To obtain $f$ at 100 m, a parameterization of $f$ is developed based on the simulations for both the cumulus and stratocumulus cases with a higher resolution of 10 m; the other configurations are the same as those in the experiment *default*. The 10 m-resolution simulation results are then averaged to the resolution of 100 m. Following Xu and Randall (1996), "1 - $f$" can be fitted by the

414    function

$$1-f=RH_{\text{grid}}^{\gamma}\left[1-\exp\left(-\beta q_{\text{c}}\right)\right], \tag{11}$$

416    where $\gamma$ and $\beta$ are empirical parameters. Figure 8 shows that the parameterization with

417    $\gamma = 8.72$ and $\beta = 1.47 \times 10^4$ can well reproduce the simulated values of "$1 - f$", with the

418    correlation coefficient ($R$) of 0.89 and significant level $p$ value < 0.01. Considering

419    that local shear ($dw/dz$) and buoyancy ($B$) may drive turbulence generation and

420    entrainment for a microscale process, the two quantities are also used to fit "$1 - f$"

421    except for RH$_{\text{grid}}$ and $q_{\text{c}}$. However, the addition of $dw/dz$ and $B$ to Equation (11) does

422    not increase $R$. Therefore, using RH$_{\text{grid}}$ and $q_{\text{c}}$ to parametrize "$1 - f$" is good and

423    reasonable for a microscale process.

424        Equations (9-11) are applied in the simulations for both the cumulus and

425    stratocumulus cases with different aerosol background (hereafter *new_f* and

426    *new_f_10*). Same as Figures 3 and 5, the temporal evolutions of the cloud physical

427    properties ($q_{\text{c}}$, $N_{\text{c}}$, $r_{\text{v}}$, CWP, and $\tau$) in *default*, *default_10*, *new_f*, and *new_f_10* are

428    shown in Figures 9 and 10. The results are similar to Figures 3 and 5. The mean values

429    of these properties of *new_f* and *new_f_10* for the cumulus and stratocumulus cases

430    are also shown in Table 6, the results of *new* and *new_10* are also shown in the

431    parentheses for the convenience of comparison. The results of *new_f* and *new* are very

432    similar, with the maximum difference being no more than 1%, so are the results of

433    tenfold aerosol background. Such a close agreement suggests that the results of the

434    new entrainment-mixing parametrization with grid-mean RH are reliable.

435    It is worth noting that instead of parameterizing $f$, Jarecka et al. (2009) and

436    Jarecka et al. (2013) added an equation to predict $f$ for each grid. In principle, this is a

437    good choice if this method is available in models. Our method shown here is an

438    alternative way to represent entrainment-mixing process when the prognostic $f$ is not

439    available.

440

441    **4. Concluding remarks**

442    The entrainment-mixing process near cloud edges has important effects on cloud

443    microphysics, but the most commonly used microphysics schemes simply assume one

444    extreme mechanism, that is, homogeneous entrainment-mixing. This study first

445    improves the entrainment-mixing parameterization proposed by Luo et al. (2020),

446    which connects the homogeneous mixing degree and transition scale number to

447    estimate the homogeneity of the subgrid mixing process and its impact on the droplet

448    number concentration. The improved parameterization uses grid-mean relative

449    humidity and can be implemented directly into microphysics schemes; there is no need

450    to know the relative humidity of the entrained air. Second, the modified entrainment-

451    mixing parameterization is implemented in the two-moment Thompson aerosol-aware

452    scheme of the LES version of WRF-Solar, to examine its effects on the microphysical

453    and optical properties of cumulus and stratocumulus clouds. Third, several sensitivity

454    experiments are conducted to investigate the effects of the new entrainment-mixing

455    parameterization under different conditions of turbulence dissipation rate and aerosol

456 number concentration. The results of implementing the new entrainment-mixing

457 parameterization are finally verified by the results using entrained air properties.

458      Unlike the commonly assumed homogeneous mixing scenario, the new

459 entrainment-mixing parameterization produces a smaller cloud droplet number

460 concentration and larger cloud droplet radius, with the degree of difference depending

461 on cloud types and stages. Sensitivity tests show that in the cumulus case, the largest

462 average influence of the new entrainment-mixing parameterization occurs under a high

463 aerosol background, but results in only a 2.74% decrease in cloud droplet number

464 concentration and a 0.57% increase in cloud droplet volume-mean radius. The changes

465 become even smaller with a low aerosol background because of the larger cloud droplet

466 radius. In contrast, the new entrainment-mixing parameterization has a larger influence

467 on the microphysical and optical properties of stratocumulus clouds, especially under a

468 high aerosol background and during the mature stage, with a cloud fraction equal to 1.

469 The largest changes resulting from the new entrainment-mixing parameterization are –

470 9.69%, +3.88%, and –5.85%, for cloud number concentration, cloud droplet volume-

471 mean radius, and cloud optical depth, respectively. The new entrainment-mixing

472 parameterization has less of an influence on the dissipation stage than on the mature

473 stage of the stratocumulus case, but affects this case more than the cumulus case.

474      The varying effects of the new entrainment-mixing parameterization are caused

475 by variations in the dominant entrainment-mixing mechanism between different cloud

476 types and stages. Compared to the cumulus case, the stratocumulus case has a much

477 smaller homogeneous mixing degree and a larger proportion of inhomogeneous mixing

478 grid points, especially during the mature stage, which indicates that the inhomogeneous

479 mixing mechanism dominates in the stratocumulus case, while the homogeneous

480 mixing mechanism dominates in the cumulus case. As mentioned above, the changes

481 in physical properties of stratocumulus clouds in the dissipation stage are between those

482 in the mature stage and those of the cumulus case; this is because stratocumulus clouds

483 dissipate sharply to form small cumulus clouds, and the degree of homogeneous mixing

484 during the dissipation stage is therefore between that which occurs during the mature

485 stage and the cumulus case.

486    Sensitivity studies show that turbulence dissipation rate and aerosol concentration

487 can have notable effects on the subgrid homogeneity of the mixing process. A larger

488 dissipation rate can accelerate the mixing process, which results in a larger transition

489 scale number and homogeneous mixing degree; and therefore, a mostly homogenous

490 mixing mechanism. This is why the cumulus case exhibit smaller changes than the

491 stratocumulus case after the new entrainment-mixing parameterization is implemented.

492 Larger aerosol number concentrations cause a smaller cloud droplet radius. Smaller

493 droplets evaporate more easily, which leads to a smaller transition scale number and a

494 smaller homogeneous mixing degree. Thus, the entrainment-mixing mechanism tends

495 to be inhomogeneous. Therefore, a larger aerosol number concentration increases the

496 influence of the new entrainment-mixing parameterization in both the cumulus and

497 stratocumulus cases.

498  The influences of implementing the new entrainment-mixing parameterization

499 with grid-mean relative humidity have been verified by simulations with entrained air

500 properties. The entrained air properties are obtained and calculated from simulations

501 with a finer resolution (10 m). Sensitivity tests show similar cloud microphysical and

502 optical properties in the two different methods, which suggests that the new

503 entrainment-mixing parameterization with grid-mean relative humidity is convincing.

504  Note that the new entrainment-mixing parameterization could be more important

505 in the models if the relative humidity near the cloud is more accurately simulated,

506 because numerical diffusion may spuriously humidify the entrained air (Hoffmann and

507 Feingold, 2019). The artificially increased relative humidity limits the influences of the

508 new entrainment-mixing parameterization, because homogeneous and inhomogeneous

509 entrainment-mixing processes are close to each other under conditions of high relative

510 humidity.

511

512 **Author contributions.** XX, CL and YL designed the experiments. XX carried out the

513 experiments and conducted the data analysis with contributions from all coauthors. XX,

514 CL, XZ, and SE developed the model code. XX prepared the paper with help from CL,

515 YL, YW, SL, and LZ.

516

517 **Competing interests.** The authors declare that they have no conflict of interest.

518

519   **Acknowledgements.** This research is supported by the National Natural Science

520   Foundation of China (41822504, 42175099, 42027804, 41975181, 42075073). Liu,

521   Zhou, and Endo are supported by the U.S. Department of Energy's Office of Energy

522   Efficiency and Renewable Energy (EERE) under Solar Energy Technologies Office

523   (SETO) Award Number 33504, and Office of Science Biological and Environmental

524   Research as part of the Atmospheric Systems Research (ASR) Program. Brookhaven

525   National Laboratory is operated by Battelle for the U.S. Department of Energy under

526   Contract DE-SC00112704. The large-scale forcing data used in this paper can be

527   downloaded from the U.S. Department of Energy's Atmospheric Radiation

528   Measurement Program with https://adc.arm.gov/discovery/#/results. The LASSO data

529   can be downloaded from https://archive.arm.gov/lassobrowser. The views expressed

530   herein do not necessarily represent the views of the U.S. Department of Energy or the

531   United States Government.

532

533   **Reference**

534   Ackerman, A. S., Kirkpatrick, M. P., Stevens, D. E., and Toon, O. B.: The impact of
535   humidity above stratiform clouds on indirect aerosol climate forcing, Nature, 432,
536   1014-1017, 2004.
537   Andrejczuk, M., Grabowski, W. W., Malinowski, S. P., and Smolarkiewicz, P. K.:
538   Numerical simulation of cloud-clear air interfacial mixing: Effects on cloud
539   microphysics, J. Atmos. Sci., 63, 3204-3225, doi:10.1175/JAS3813.1, 2006.
540   Andrejczuk, M., Grabowski, W. W., Malinowski, S. P., and Smolarkiewicz, P. K.:
541   Numerical simulation of cloud–clear air interfacial mixing: Homogeneous versus
542   inhomogeneous mixing, J. Atmos. Sci., 66, 2493-2500, doi:10.1175/2009JAS2956.1,
543   2009.
544   Burnet, F. and Brenguier, J. L.: Observational study of the entrainment-mixing process
545   in warm convective clouds, J. Atmos. Sci., 64, 1995-2011, doi:10.1175/JAS3928.1,

546 2007.

547 Chosson, F., Brenguier, J.-L., and Schüller, L.: Entrainment-mixing and radiative
548 transfer simulation in boundary layer clouds, J. Atmos. Sci., 64, 2670-2682,
549 doi:10.1175/JAS3975.1, 2007.

550 Deardorff, J.: Stratocumulus-capped mixed layers derived from a three-dimensional
551 model, Boundary-Layer Meteorol, 18, 495-527, 10.1007/BF00119502, 1980.

552 Del Genio, A. D. and Wu, J.: The role of entrainment in the diurnal cycle of continental
553 convection, J. Climate, 23, 2722-2738, doi: 10.1175/2009JCLI3340.1, 2010.

554 Endo, S., Fridlind, A. M., Lin, W., Vogelmann, A. M., Toto, T., Ackerman, A. S.,
555 McFarquhar, G. M., Jackson, R. C., Jonsson, H. H., and Liu, Y.: RACORO continental
556 boundary layer cloud investigations: 2. Large‐eddy simulations of cumulus clouds
557 and evaluation with in situ and ground‐based observations, Journal of Geophysical
558 Research: Atmospheres, 120, 5993-6014, 2015.

559 Fan, J., Wang, Y., Rosenfeld, D., and Liu, X.: Review of Aerosol–Cloud Interactions:
560 Mechanisms, Significance, and Challenges, Journal of the Atmospheric Sciences, 73,
561 4221-4252, 10.1175/jas-d-16-0037.1, 2016.

562 Freud, E., Rosenfeld, D., and Kulkarni, J. R.: Resolving both entrainment-mixing and
563 number of activated CCN in deep convective clouds, Atmos. Chem. Phys., 11, 12887-
564 12900, 2011.

565 Freud, E., Rosenfeld, D., Andreae, M. O., Costa, A. A., and Artaxo, P.: Robust relations
566 between CCN and the vertical evolution of cloud drop size distribution in deep
567 convective clouds, Atmos. Chem. Phys., 8, 1661-1675, 2008.

568 Gao, S., Lu, C., Liu, Y., Mei, F., Wang, J., Zhu, L., and Yan, S.: Contrasting Scale
569 Dependence of Entrainment‐Mixing Mechanisms in Stratocumulus Clouds,
570 Geophysical Research Letters, 47, 10.1029/2020gl086970, 2020.

571 Gao, S., Lu, C., Liu, Y., Yum, S. S., Zhu, J., Zhu, L., Desai, N., Ma, Y., and Wu, S.:
572 Comprehensive quantification of height dependence of entrainment mixing between
573 stratiform cloud top and environment, Atmospheric Chemistry and Physics, 21, 11225-
574 11241, 2021.

575 Gao, Z., Liu, Y., Li, X., and Lu, C.: Investigation of Turbulent Entrainment-Mixing
576 Processes with a New Particle-Resolved Direct Numerical Simulation Model, J.
577 Geophys. Res., 123, 2194-2214, 2018.

578 Gerber, H. E., Frick, G. M., Jensen, J. B., and Hudson, J. G.: Entrainment, mixing, and
579 microphysics in trade-wind cumulus, J. Meteorol. Soc. Japan, 86A, 87-106, 2008.

580 Grabowski, W. W.: Indirect impact of atmospheric aerosols in idealized simulations of
581 convective-radiative quasi equilibrium, J. Climate, 19, 4664-4682,
582 doi:10.1175/JCLI3857.1, 2006.

583 Grabowski, W. W.: Representation of turbulent mixing and buoyancy reversal in bulk
584 cloud models, Journal of the atmospheric sciences, 64, 3666-3680, 2007.

585 Grabowski, W. W. and Morrison, H.: Indirect Impact of Atmospheric Aerosols in
586 Idealized Simulations of Convective–Radiative Quasi Equilibrium. Part II: Double-
587 Moment Microphysics, Journal of Climate, 24, 1897-1912, 10.1175/2010jcli3647.1,

588     2011.

589     Gustafson, W. I., Vogelmann, A. M., Li, Z., Cheng, X., Dumas, K. K., Endo, S., Johnson,
590     K. L., Krishna, B., Fairless, T., and Xiao, H.: The Large-Eddy Simulation (LES)
591     Atmospheric Radiation Measurement (ARM) Symbiotic Simulation and Observation
592     (LASSO) Activity for Continental Shallow Convection, Bulletin of the American
593     Meteorological Society, 101, E462-E479, 10.1175/bams-d-19-0065.1, 2020.

594     Hacker, J. P., Jimenez, P. A., Dudhia, J., Haupt, S. E., Ruiz-Arias, J. A., Gueymard, C.
595     A., Thompson, G., Eidhammer, T., and Deng, A.: WRF-Solar: Description and Clear-
596     Sky Assessment of an Augmented NWP Model for Solar Power Prediction, Bulletin of
597     the American Meteorological Society, 97, 1249-1264, 10.1175/bams-d-14-00279.1,
598     2016.

599     Haman, K. E., Malinowski, S. P., Kurowski, M. J., Gerber, H., and Brenguier, J.-L.:
600     Small scale mixing processes at the top of a marine stratocumulus - a case study, Q. J.
601     Roy. Meteor. Soc., 133, 213-226, doi:10.1002/qj.5, 2007.

602     Haupt, S. E., Kosovic, B., Jensen, T., Lee, J., Jimenez, P., Lazo, J., Cowie, J.,
603     McCandless, T., Pearson, J., and Weiner, G.: The SunCast□ solar-power forecasting
604     system: the results of the public-private-academic partnership to advance solar power
605     forecasting, National Center for Atmospheric Research (NCAR), Boulder (CO):
606     Research Applications Laboratory, Weather Systems and Assessment Program (US),
607     2016.

608     Hill, A. A., Feingold, G., and Jiang, H.: The influence of entrainment and mixing
609     assumption on aerosol-cloud interactions in marine stratocumulus, J. Atmos. Sci., 66,
610     1450-1464, 2009.

611     Hoffmann, F. and Feingold, G.: Entrainment and mixing in stratocumulus: Effects of a
612     new explicit subgrid-scale scheme for large-eddy simulations with particle-based
613     microphysics, J. Atmos. SCi., 76, 1955-1973, 10.1175/jas-d-18-0318.1, 2019.

614     Hoffmann, F., Yamaguchi, T., and Feingold, G.: Inhomogeneous mixing in Lagrangian
615     cloud models: Effects on the production of precipitation embryos, Journal of the
616     Atmospheric Sciences, 76, 113-133, 2019.

617     Huang, J., Lee, X., and Patton, E. G.: A modelling study of flux imbalance and the
618     influence of entrainment in the convective boundary layer, Boundary-layer meteorology,
619     127, 273-292, 2008.

620     Jarecka, D., Grabowski, W. W., and Pawlowska, H.: Modeling of Subgrid-Scale Mixing
621     in Large-Eddy Simulation of Shallow Convection, Journal of the Atmospheric Sciences,
622     66, 2125-2133, 10.1175/2009jas2929.1, 2009.

623     Jarecka, D., Grabowski, W. W., Morrison, H., and Pawlowska, H.: Homogeneity of the
624     subgrid-scale turbulent mixing in large-eddy simulation of shallow convection, J.
625     Atmos. Sci., 70, 2751-2767, 2013.

626     Jensen, J. B., Austin, P. H., Baker, M. B., and Blyth, A. M.: Turbulent mixing, spectral
627     evolution and dynamics in a warm cumulus cloud, J. Atmos. Sci., 42, 173-192,
628     doi:10.1175/1520-0469(1985)042<0173:TMSEAD>2.0.CO;2, 1985.

629     Kim, B.-G., Miller, M. A., Schwartz, S. E., Liu, Y., and Min, Q.: The role of adiabaticity

in the aerosol first indirect effect, J. Geophys. Res., 113, D05210, doi: 10.1029/2007jd008961, 2008.

Kumar, B., Schumacher, J., and Shaw, R.: Cloud microphysical effects of turbulent mixing and entrainment, Theor. Comp. Fluid Dyn., 27, 361-376, 2013.

Lasher-Trapp, S. G., Cooper, W. A., and Blyth, A. M.: Broadening of droplet size distributions from entrainment and mixing in a cumulus cloud, Q. J. Roy. Meteor. Soc., 131, 195-220, doi:10.1256/qj.03.199, 2005.

Lehmann, K., Siebert, H., and Shaw, R. A.: Homogeneous and inhomogeneous mixing in cumulus clouds: dependence on local turbulence structure, J. Atmos. Sci., 66, 3641-3659, doi:10.1175/2009JAS3012.1, 2009.

Li, Z., Li, C., Chen, H., Tsay, S. C., Holben, B., Huang, J., Li, B., Maring, H., Qian, Y., and Shi, G.: East Asian studies of tropospheric aerosols and their impact on regional climate (EAST‐AIRC): An overview, Journal of Geophysical Research: Atmospheres, 116, 2011.

Lu, C., Liu, Y., and Niu, S.: Examination of turbulent entrainment-mixing mechanisms using a combined approach, J. Geophys. Res., 116, D20207, doi:10.1029/2011JD015944, 2011.

Lu, C., Liu, Y., Niu, S., and Endo, S.: Scale dependence of entrainment‐mixing mechanisms in cumulus clouds, Journal of Geophysical Research: Atmospheres, 119, 13,877-813,890, 2014.

Lu, C., Liu, Y., Niu, S., Krueger, S., and Wagner, T.: Exploring parameterization for turbulent entrainment-mixing processes in clouds, Journal of Geophysical Research: Atmospheres, 118, 185-194, 10.1029/2012jd018464, 2013.

Lu, C., Liu, Y., Zhang, G. J., Wu, X., Endo, S., Cao, L., Li, Y., and Guo, X.: Improving parameterization of entrainment rate for shallow convection with aircraft measurements and large eddy simulation, J. Atmos. Sci., 73, 761-773, 10.1175/JAS-D-15-0050.1, 2016.

Luo, S., Lu, C., Liu, Y., Bian, J., Gao, W., Li, J., Xu, X., Gao, S., Yang, S., and Guo, X.: Parameterizations of Entrainment‐Mixing Mechanisms and Their Effects on Cloud Droplet Spectral Width Based on Numerical Simulations, Journal of Geophysical Research: Atmospheres, 125, e2020JD032972, 2020.

Morrison, H. and Grabowski, W. W.: Modeling supersaturation and subgrid-scale mixing with two-moment bulk warm microphysics, J. Atmos. Sci., 65, 792-812, doi:10.1175/2007JAS2374.1, 2008.

Paluch, I. R. and Baumgardner, D. G.: Entrainment and fine-scale mixing in a continental convective cloud, J. Atmos. Sci., 46, 261-278, doi:10.1175/1520-0469(1989)046<0261:EAFSMI>2.0.CO;2, 1989.

Pawlowska, H., Brenguier, J. L., and Burnet, F.: Microphysical properties of stratocumulus clouds, Atmos. Res., 55, 15-33, 2000.

Peng, Y., Lohmann, U., Leaitch, R., Banic, C., and Couture, M.: The cloud albedo-cloud droplet effective radius relationship for clean and polluted clouds from RACE and FIRE.ACE, J. Geophys. Res., 107, AAC 1-1-AAC 1-6, 10.1029/2000JD000281, 2002.

672 Slawinska, J., Grabowski, W. W., Pawlowska, H., and Morrison, H.: Droplet activation
673 and mixing in large-eddy simulation of a shallow cumulus field, J. Atmos. Sci., 69, 444-
674 462, 2012.

675 Slawinska, J., Grabowski, W. W., Pawlowska, H., and Wyszogrodzki, A. A.: Optical
676 properties of shallow convective clouds diagnosed from a bulk-microphysics large-
677 eddy simulation, J. Climate, 21, 1639-1647, 2008.

678 Small, J. D., Chuang, P., and Jonsson, H.: Microphysical imprint of entrainment in
679 warm cumulus, Tellus B, 65, 6647-6662, 2013.

680 Thompson, G. and Eidhammer, T.: A study of aerosol impacts on clouds and
681 precipitation development in a large winter cyclone, Journal of the atmospheric
682 sciences, 71, 3636-3658, 2014.

683 Wang, H. and Feingold, G.: Modeling mesoscale cellular structures and drizzle in
684 marine stratocumulus. Part I: Impact of drizzle on the formation and evolution of open
685 cells, Journal of the Atmospheric Sciences, 66, 3237-3256, 2009.

686 Wang, M., Ghan, S., Ovchinnikov, M., Liu, X., Easter, R., Kassianov, E., Qian, Y., and
687 Morrison, H.: Aerosol indirect effects in a multi-scale aerosol-climate model PNNL-
688 MMF, Atmospheric Chemistry and Physics, 11, 5431-5455, 2011.

689 Wang, Y., Zhao, C., McFarquhar, G. M., Wu, W., Reeves, M., and Li, J.: Dispersion of
690 Droplet Size Distributions in Supercooled Non‐precipitating Stratocumulus from
691 Aircraft Observations Obtained during the Southern Ocean Cloud Radiation Aerosol
692 Transport Experimental Study, Journal of Geophysical Research: Atmospheres, 126,
693 e2020JD033720, 2021.

694 Wang, Y., Niu, S., Lv, J., Lu, C., Xu, X., Wang, Y., Ding, J., Zhang, H., Wang, T., and
695 Kang, B.: A new method for distinguishing unactivated particles in cloud condensation
696 nuclei measurements: Implications for aerosol indirect effect evaluation, Geophysical
697 Research Letters, 46, 14185-14194, 2019.

698 Wood, R.: Review: Stratocumulus Clouds, Monthly Weather Review, 140, 2373-2423,
699 2012.

700 Xu, K.-M. and Randall, D. A.: A semiempirical cloudiness parameterization for use in
701 climate models, Journal of the atmospheric sciences, 53, 3084-3102, 1996.

702 Xu, X., Sun, C., Lu, C., Liu, Y., Zhang, G. J., and Chen, Q.: Factors affecting
703 entrainment rate in deep convective clouds and parameterizations, Journal of
704 Geophysical Research: Atmospheres, 126, e2021JD034881, 2021.

705 Xu, X., Lu, C., Liu, Y., Gao, W., Wang, Y., Cheng, Y., Luo, S., and Van Weverberg, K.:
706 Effects of cloud liquid‐phase microphysical processes in mixed‐phase cumuli over
707 the Tibetan Plateau, Journal of Geophysical Research: Atmospheres, 125,
708 e2020JD033371, 2020.

709 Yang, B., Wang, M., Zhang, G. J., Guo, Z., Huang, A., Zhang, Y., and Qian, Y.: Linking
710 Deep and Shallow Convective Mass Fluxes via an Assumed Entrainment Distribution
711 in CAM5‐CLUBB: Parameterization and Simulated Precipitation Variability, Journal
712 of Advances in Modeling Earth Systems, 13, e2020MS002357, 2021.

713 Yang, F., Shaw, R., and Xue, H.: Conditions for super-adiabatic droplet growth after

714  entrainment mixing, Atmos. Chem. Phys., 16, 9421-9433, 10.5194/acp-2016-94, 2016.

715  Yum, S.: Cloud droplet spectral broadening in warm clouds: An observational and

716  model study, Dissertation for the Doctoral Degree, University of Nevada, Reno, Nevada,

717  USA, 191 pp., 1998.

718  Zhang, M. H., Lin, J. L., Cederwall, R. T., Yio, J. J., and Xie, S. C.: Objective analysis

719  of ARM IOP data: Method and sensitivity, Mon. Weather Rev., 129, 295-311,

720  10.1175/1520-0493(2001)129<0295:OAOAID>2.0.CO;2, 2001.

721  Zheng, Y. and Rosenfeld, D.: Linear relation between convective cloud base height and

722  updrafts and application to satellite retrievals, Geophysical Research Letters, 42, 6485-

723  6491, 10.1002/2015gl064809, 2015.

724  Zheng, Y., Rosenfeld, D., and Li, Z.: Quantifying cloud base updraft speeds of marine

725  stratocumulus from cloud top radiative cooling, Geophysical Research Letters, 43,

726  11,407-411,413, 2016.

727  Zhu, L., Lu, C., Yan, S., Liu, Y., Zhang, G. J., Mei, F., Zhu, B., Fast, J. D., Matthews,

728  A., and Pekour, M. S.: A New Approach for Simultaneous Estimation of Entrainment

729  and Detrainment Rates in Non‐Precipitating Shallow Cumulus, Geophysical Research

730  Letters, 48, 10.1029/2021gl093817, 2021.

731

732

733    Table 1. Summary of names and corresponding descriptions of the four experiments for

734    each case of cumulus and stratocumulus. The meaning of each symbol for each

735    experiment can be found in the text.

| | Entrainment-mixing parameterization | Dissipation rate | Aerosol number concentration |
|---|---|---|---|
| *default* | $\alpha = 0$ | - | default |
| *new* | $\alpha = 1 - \psi,$ $\psi = 107.19\exp(-1.99 N_{\mathrm{L}}^{-0.29}).$ | $\varepsilon = CE^{3/2}/L.$ | default |
| *default_10* | $\alpha = 0$ | - | default×10 |
| *new_10* | $\alpha = 1 - \psi,$ $\psi = 107.19\exp(-1.99 N_{\mathrm{L}}^{-0.29}).$ | $\varepsilon = CE^{3/2}/L.$ | default×10 |

736

737 Table 2. Summary of the case mean values of the key quantities in all the simulations

738 of the cumulus case, containing cloud water mixing ratio ($q_c$), cloud droplet number

739 concentration ($N_c$), cloud droplet volume-mean radius ($r_v$), cloud water path (CWP),

740 and cloud optical depth ($\tau$). The experiments are detailed in Table 1.

|  | *default* | *new* | *default_10* | *new_10* |
|---|---|---|---|---|
| $q_c$(g/kg) | 0.44 | 0.44 | 0.56 | 0.57 |
| $N_c$(cm$^{-3}$) | 35.78 | 35.53 | 278.80 | 271.16 |
| $r_v$(μm) | 13.27 | 13.29 | 7.05 | 7.09 |
| CWP(g/m$^2$) | 142.30 | 144.25 | 186.52 | 187.13 |
| $\tau$ | 13.07 | 13.02 | 31.29 | 31.11 |

741

742

743    Table 3. Summary of the case mean values of the key quantities in all the simulations

744    of the stratocumulus case, including cloud water mixing ratio ($q_c$), cloud droplet number

745    concentration ($N_c$), cloud droplet volume-mean radius ($r_v$), cloud water path (CWP),

746    and cloud optical depth ($\tau$). The numbers in and out of the parentheses are the results at

747    the mature and dissipation stages, respectively. The experiments are detailed in Table 1.

|  | *default* | *new* | *default_10* | *new_10* |
|---|---|---|---|---|
| $q_c$(g/kg) | 0.13 | 0.13 | 0.16 | 0.16 |
|  | (0.039) | (0.039) | (0.041) | (0.041) |
| $N_c$(cm$^{-3}$) | 35.74 | 33.11 | 256.82 | 231.93 |
|  | (19.76) | (18.82) | (138.74) | (126.90) |
| $r_v$(μm) | 10.32 | 10.65 | 5.15 | 5.35 |
|  | (7.53) | (7.69) | (4.02) | (4.14) |
| CWP(g/m$^2$) | 41.39 | 41.78 | 56.21 | 57.03 |
|  | (2.57) | (2.43) | (2.71) | (2.77) |
| $\tau$ | 4.68 | 4.40 | 13.17 | 12.40 |
|  | (0.39) | (0.38) | (0.78) | (0.78) |

748

749 Table 4. Cloud water mixing ratio ($q_c$), cloud droplet number concentration ($N_c$), cloud

750 droplet volume-mean radius ($r_v$), cloud water path (CWP), cloud optical depth ($\tau$) in all

751 simulations for the entire lifetime of the stratocumulus case. The experiments are

752 detailed in Table 1.

|  | *default* | *new* | *default_10* | *new_10* |
|---|---|---|---|---|
| $q_c$(g/kg) | 0.11 | 0.11 | 0.13 | 0.13 |
| $N_c$(cm$^{-3}$) | 29.98 | 28.12 | 223.65 | 203.50 |
| $r_v$(μm) | 9.38 | 9.57 | 5.06 | 5.22 |
| CWP(g/m$^2$) | 30.78 | 29.92 | 42.22 | 43.13 |
| $\tau$ | 4.02 | 3.89 | 10.39 | 9.96 |

753

754

755 Table 5. Homogeneous mixing degree ($\psi$) at all grid points experiencing evaporation,

756 the proportion of inhomogeneous mixing grid points to all grid points experiencing

757 evaporation, and $\psi$ at the inhomogeneous mixing grid points in the experiments *new*

758 and *new_10* (Table 1) for the cumulus (Cu) and stratocumulus (St) cases. The numbers

759 in and out of the parentheses are the results at the mature and dissipation stages in the

760 stratocumulus (St) case, respectively. The experiments are detailed in Table 1.

|  | $\psi$ at all grids (%) | Proportion of inhomogeneous mixing grids (%) | $\psi$ at the inhomogeneous mixing grids (%) |
|---|---|---|---|
| *new* (Cu) | 99.93 | 4.52 | 98.62 |
| *new_10* (Cu) | 95.33 | 25.10 | 92.96 |
| *new* (St) | 78.56 | 63.07 | 71.56 |
|  | (94.68) | (40.61) | (89.33) |
| *new_10* (St) | 68.20 | 97.31 | 65.01 |
|  | (88.11) | (73.54) | (84.99) |

761

762

763 Table 6. Cloud water mixing ratio ($q_c$), cloud droplet number concentration ($N_c$), cloud

764 droplet volume-mean radius ($r_v$), cloud water path (CWP), cloud optical depth ($\tau$) in

765 *new_f* and *new_f_10* for the cumulus (Cu) and stratocumulus (Sc) cases. The results of

766 *new* and *new_10* in Tables 2 and 4 are shown in the parentheses.

| | Cu | | Sc | |
|---|---|---|---|---|
| | *new_f* | *new_f_10* | *new_f* | *new_f_10* |
| | (*new*) | (*new_10*) | (*new*) | (*new_10*) |
| $q_c$(g/kg) | 0.44 | 0.57 | 0.11 | 0.13 |
| | (0.44) | (0.57) | (0.11) | (0.13) |
| $N_c$(cm$^{-3}$) | 35.52 | 270.56 | 28.08 | 202.99 |
| | (35.53) | (271.16) | (28.12) | (203.50) |
| $r_v$(μm) | 13.30 | 7.10 | 9.60 | 5.21 |
| | (13.29) | (7.09) | (9.57) | (5.22) |
| CWP(g/m$^2$) | 143.15 | 185.95 | 30.16 | 43.32 |
| | (144.25) | (187.13) | (29.92) | (43.13) |
| $\tau$ | 13.00 | 31.08 | 3.89 | 9.93 |
| | (13.02) | (31.11) | (3.89) | (9.96) |

767

768

769
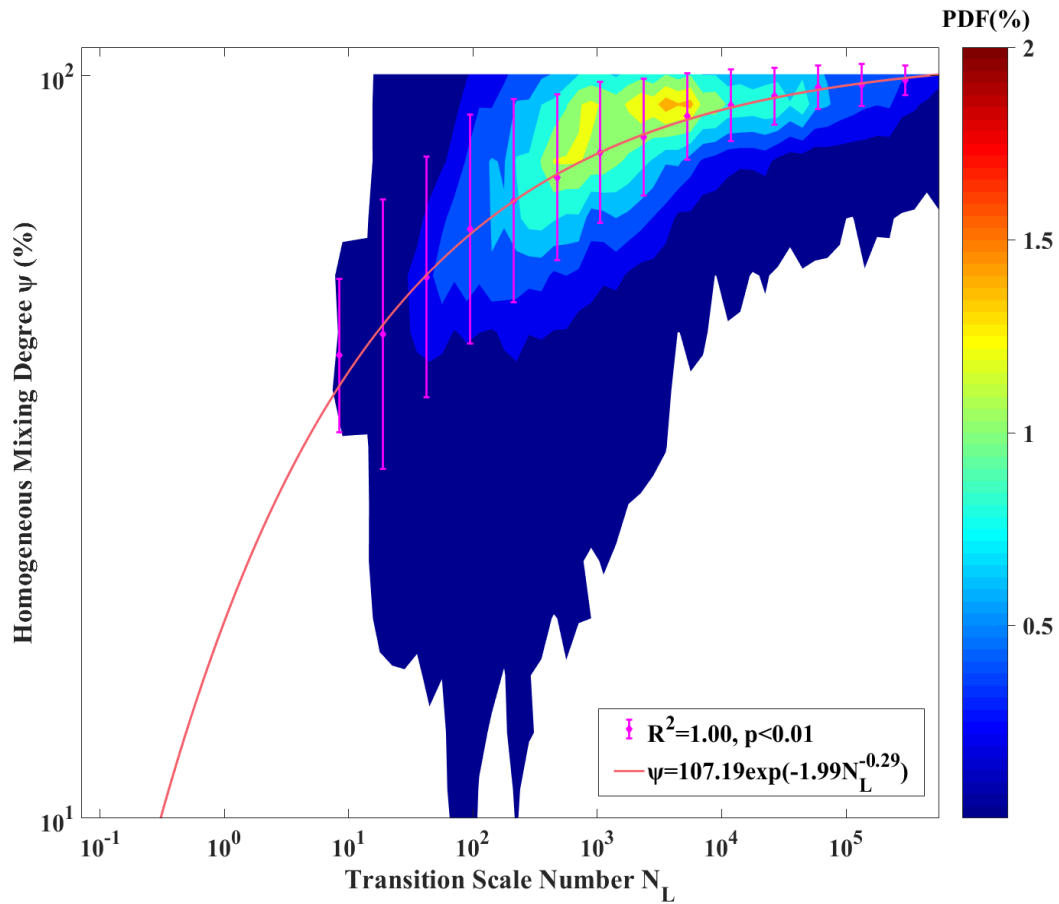
Figure 1. Parameterization of cloud entrainment-mixing mechanisms by relating

homogeneous mixing degree ($\psi$) to transition scale number ($N_L$) from EMPM. The

contours represent the joint probability distribution function (PDF) of $\psi$ vs $N_L$. The

magenta dots and error bars are mean values and standard deviations of $\psi$ in each $N_L$

bin, respectively. The mean values are fitted using a weighted least squares method with

the number of data points in each $N_L$ bin as the weight. The fitting equation, coefficient

of determination ($R^2$), and $p$-value are also given. $N_L$ is calculated by with the domain-

averaged relative humidity after entrainment but before evaporation in the EMPM.
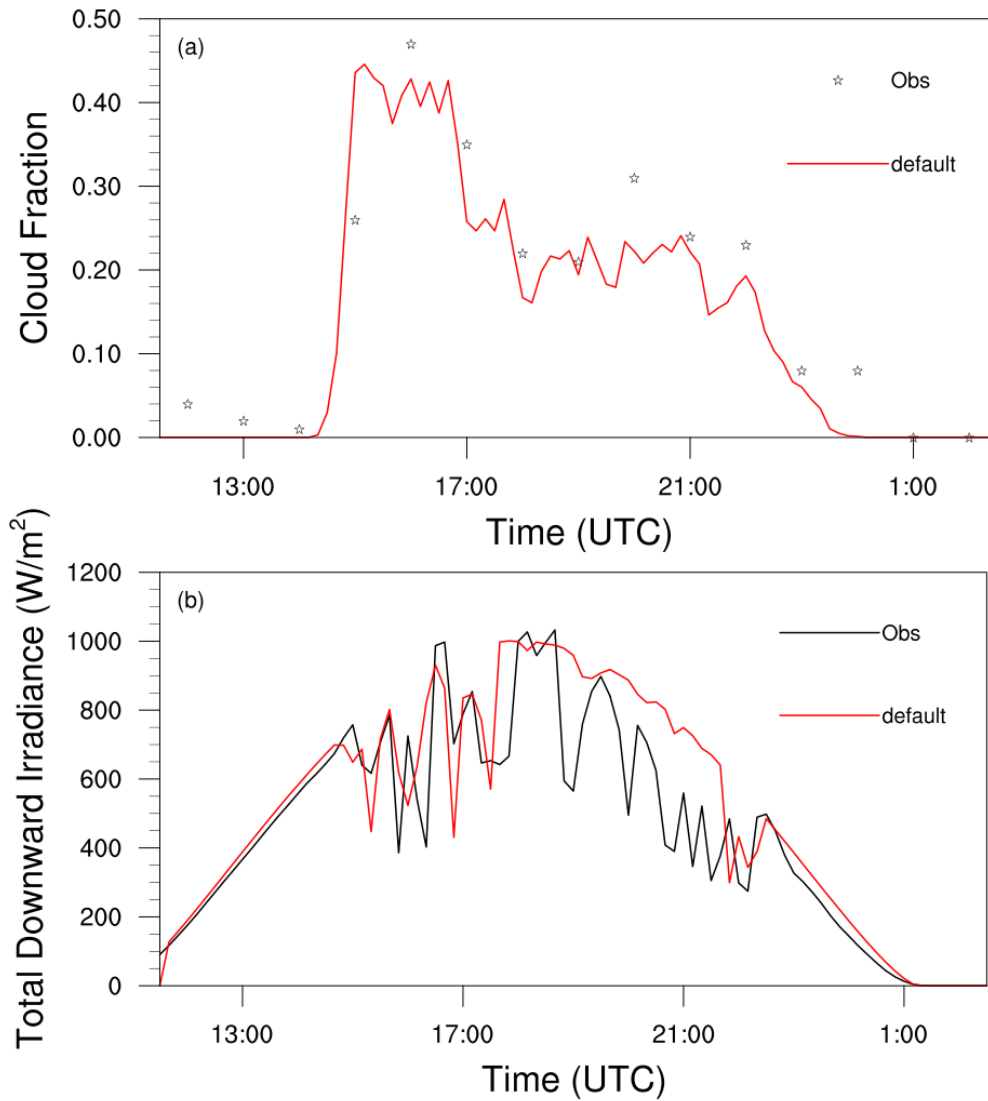
778

779     Figure 2. Time series of (a) domain-averaged cloud fraction and (b) total downward

780     irradiance at the central point from the observation and the *default* experiment in the

781     cumulus case.

782
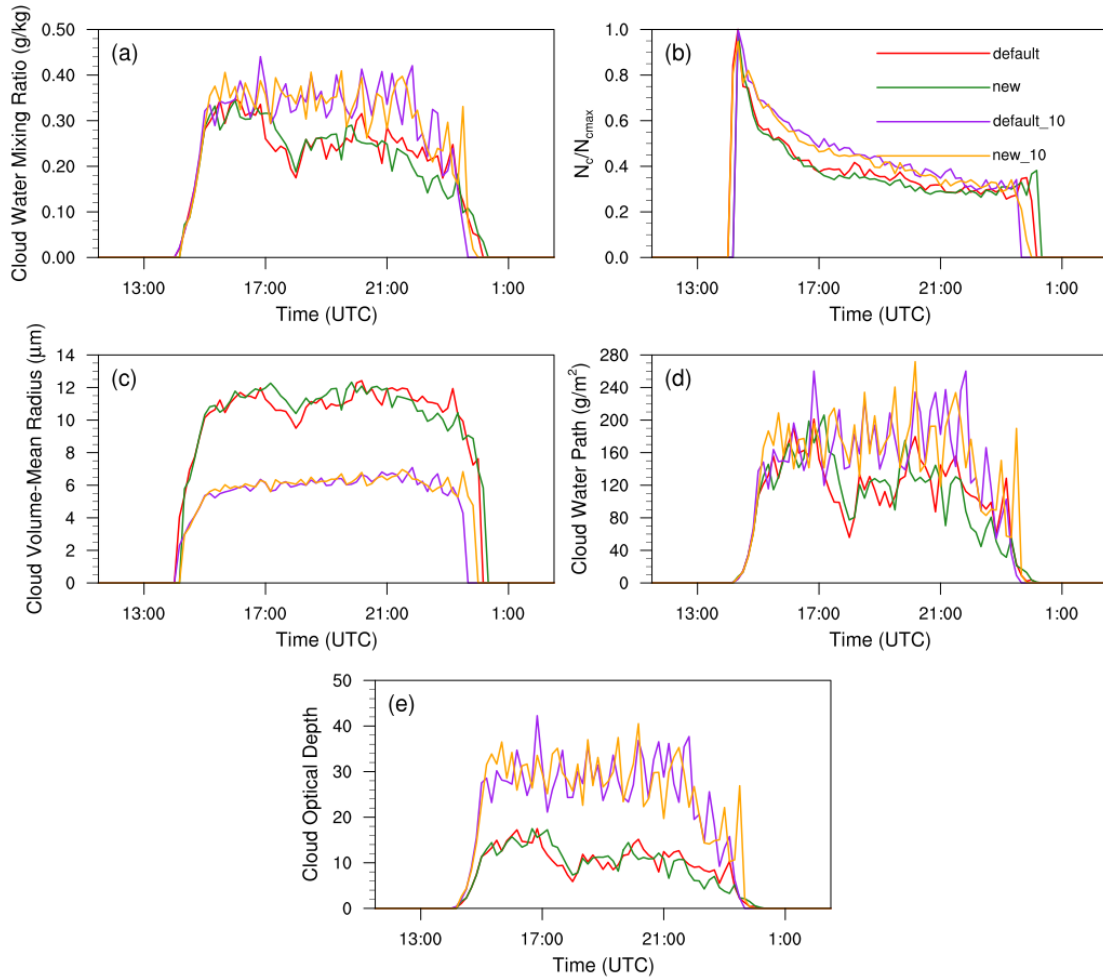
783

784 Figure 3. The temporal evolutions of main cloud microphysical and optical properties

785 in all simulation experiments for the cumulus case, including (a) cloud water mixing

786 ratio ($q_c$) (g/kg), (b) cloud droplet number concentration ($N_c$) (/cm$^3$), (c) cloud droplet

787 volume-mean radius ($r_v$) (μm), (d) cloud water path (CWP) (g/m$^2$), and (e) cloud optical

788 depth ($\tau$). In (b), $N_c$ in the experiments *default* and *new* are normalized by the maximum

789 cloud droplet concentration ($N_{cmax}$) from *default*, respectively; $N_c$ in the experiments

790 *default_10* and *new_10* are normalized by $N_{cmax}$ from *default_10*, respectively. The four

791 experiments are detailed in Table 1.
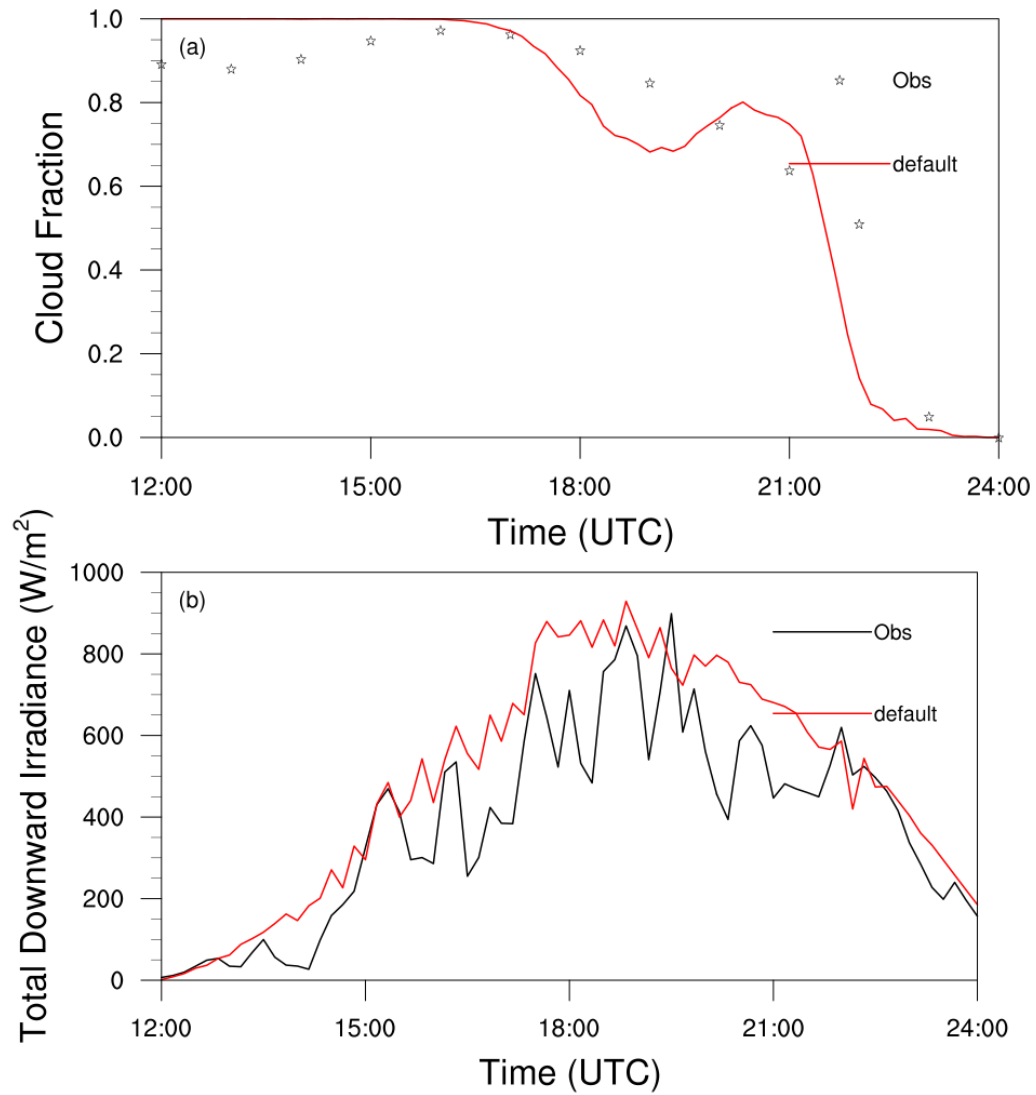
792

793 Figure 4. Time series of (a) domain-averaged cloud fraction and (b) total downward

794 irradiance at the central point from the observation and the *default* experiment in the

795 stratocumulus case.
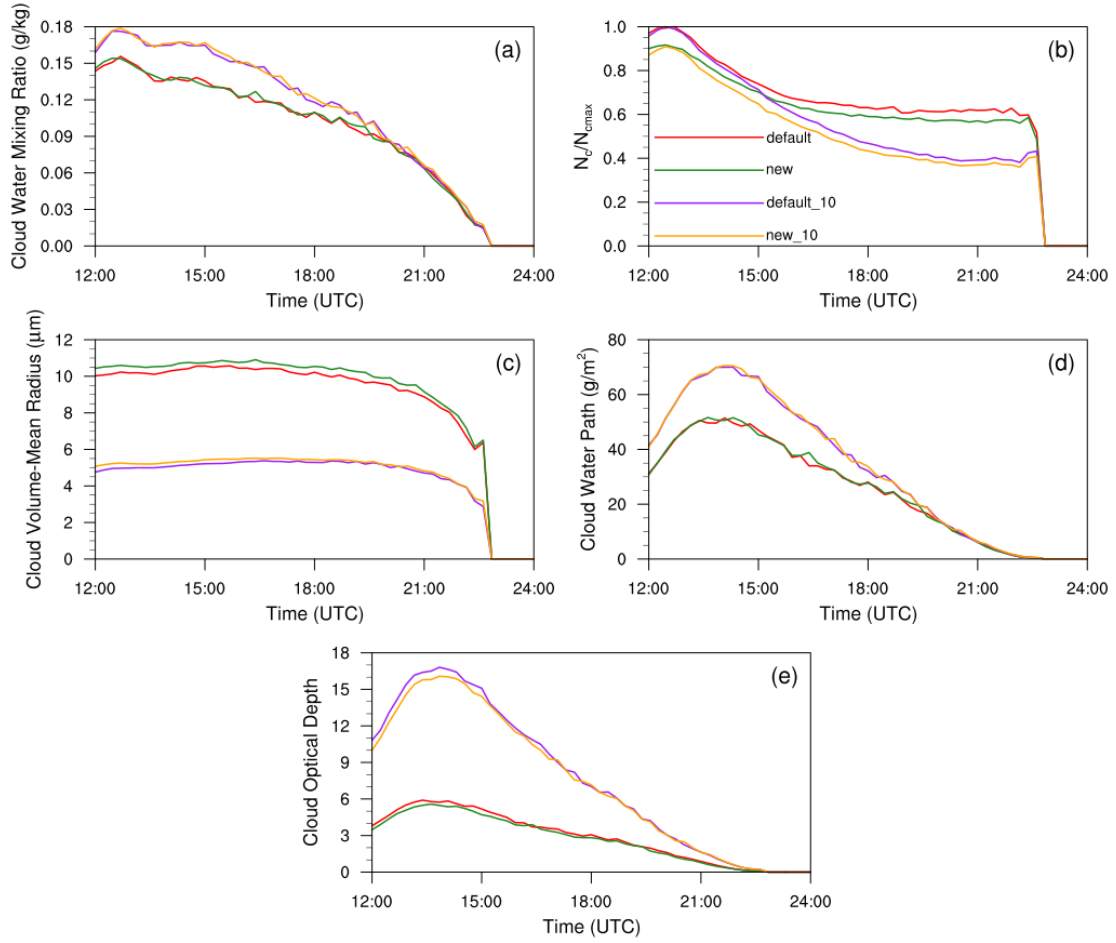
796

797 Figure 5. The temporal evolutions of main cloud microphysical and optical properties

798 in all simulation experiments for the stratocumulus case, including (a) cloud water

799 mixing ratio ($q_c$) (g/kg), (b) cloud droplet number concentration ($N_c$) (/cm$^3$), (c) cloud

800 droplet volume-mean radius ($r_v$) (μm), (d) cloud water path (CWP) (g/m$^2$), and (e) cloud

801 optical depth ($\tau$). In (b), $N_c$ in the experiments *default* and *new* are normalized by the

802 maximum cloud droplet number concentration ($N_{cmax}$) from *default*, respectively; $N_c$ in

803 the experiments *default_10* and *new_10* are normalized by $N_{cmax}$ from *default_10*,

804 respectively. The four experiments are detailed in Table 1.
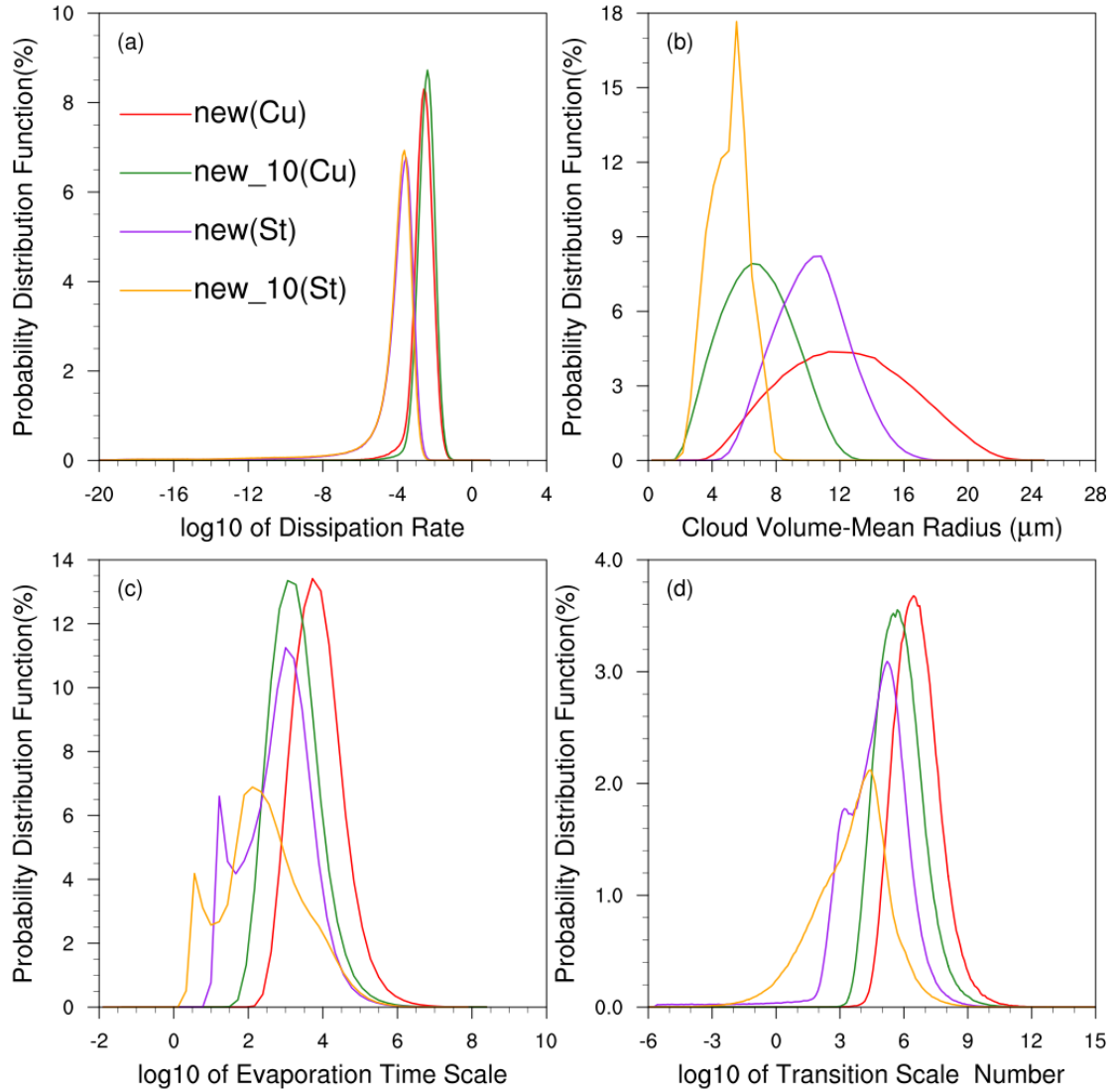
805

806 Figure 6. Probability distribution functions (PDFs) of (a) turbulence dissipation rate ($\varepsilon$),

807 (b) cloud droplet volume-mean radius ($r_v$), (c) evaporation time scale ($\tau_{evap}$), and (d)

808 transition scale number ($N_L$) of cloud grids experiencing the entrainment-mixing

809 process in the simulations with the new entrainment-mixing parameterization for the

810 cumulus case (Cu, the solid lines) and the stratocumulus case (St, the dash lines),

811 respectively. The experiments are detailed in Table 1.
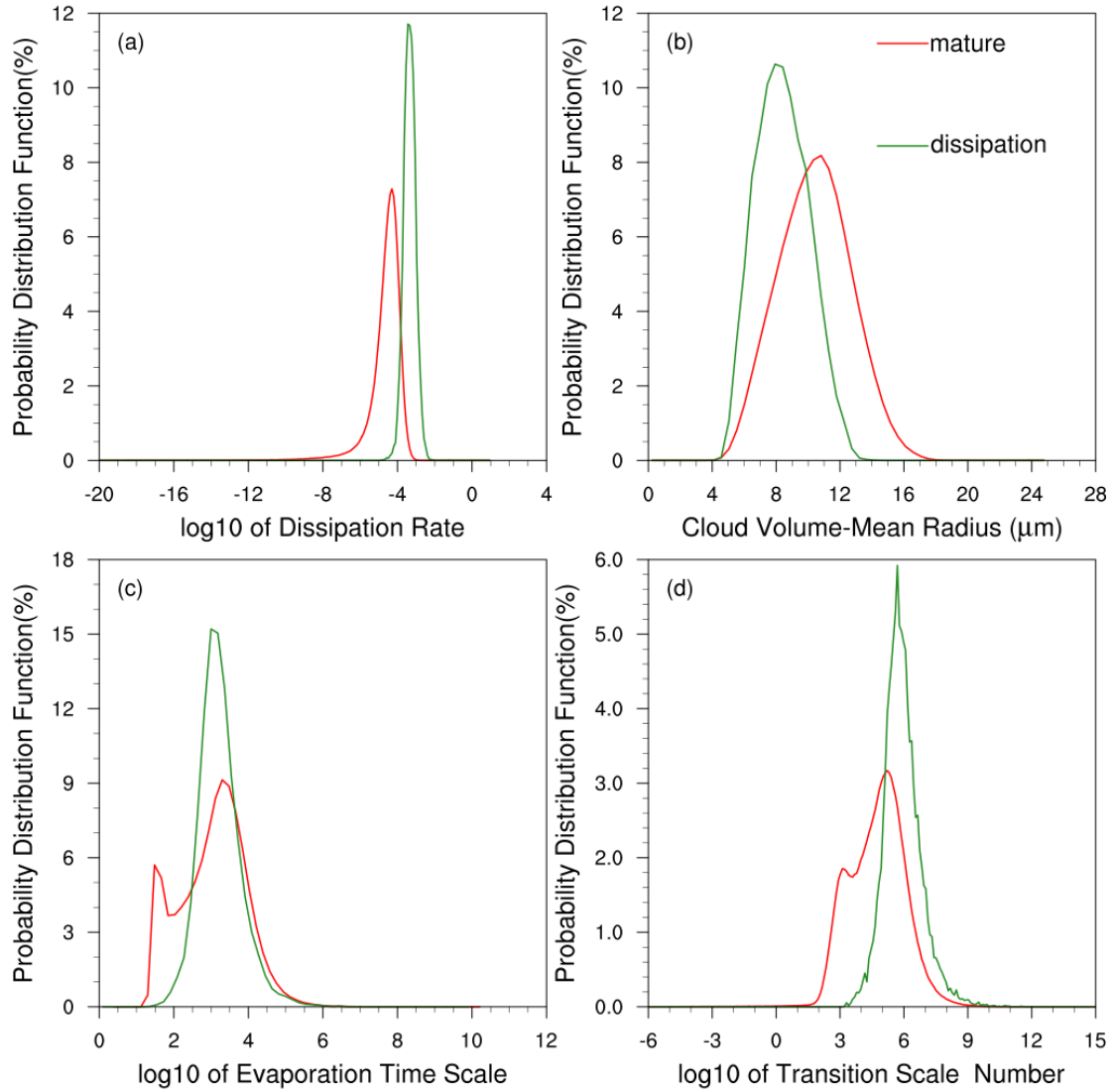
812

813 Figure 7. Probability distribution functions (PDFs) of (a) turbulence dissipation rate ($\varepsilon$),

814 (b) cloud droplet volume-mean radius ($r_v$), (c) evaporation time scale ($\tau_{evap}$), and (d)

815 transition scale number ($N_L$) of cloud grids experiencing the entrainment-mixing

816 process at the mature stage from 12:00 UTC to 16:00 UTC (the red lines) and the

817 dissipation stage from 21:00 UTC to 24:00 UTC (the green lines) in *new* for the

818 stratocumulus case. The experiment is detailed in Table 1.

819
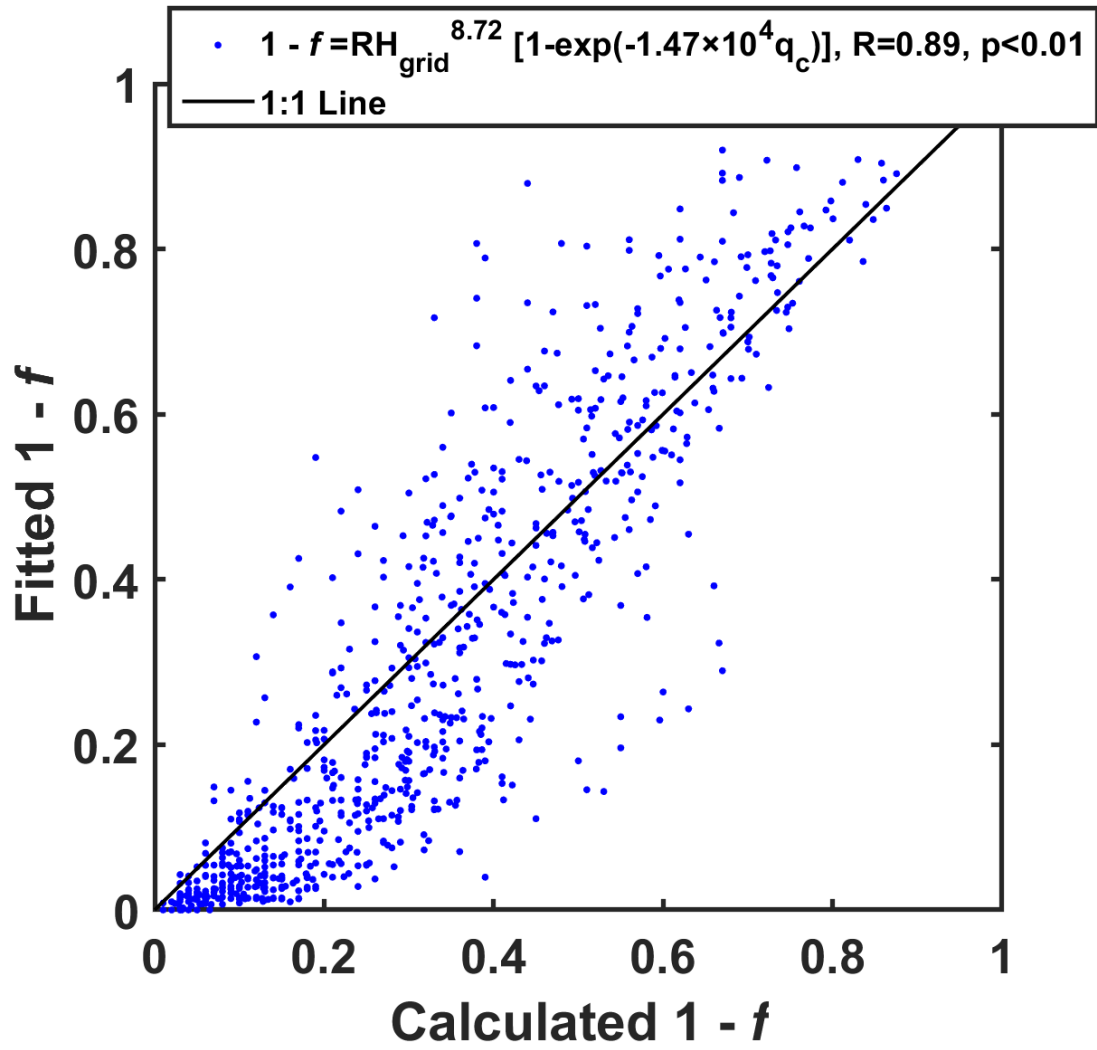
Figure 8. The fitted 1 - $f$ as a function of the calculated 1 - $f$. The fitted 1 – $f$ is obtained

by the fitting functions with grid-mean relative humidity ($RH_{grid}$) and cloud water

mixing ratio ($q_c$). The black line denotes the 1:1 line.

823
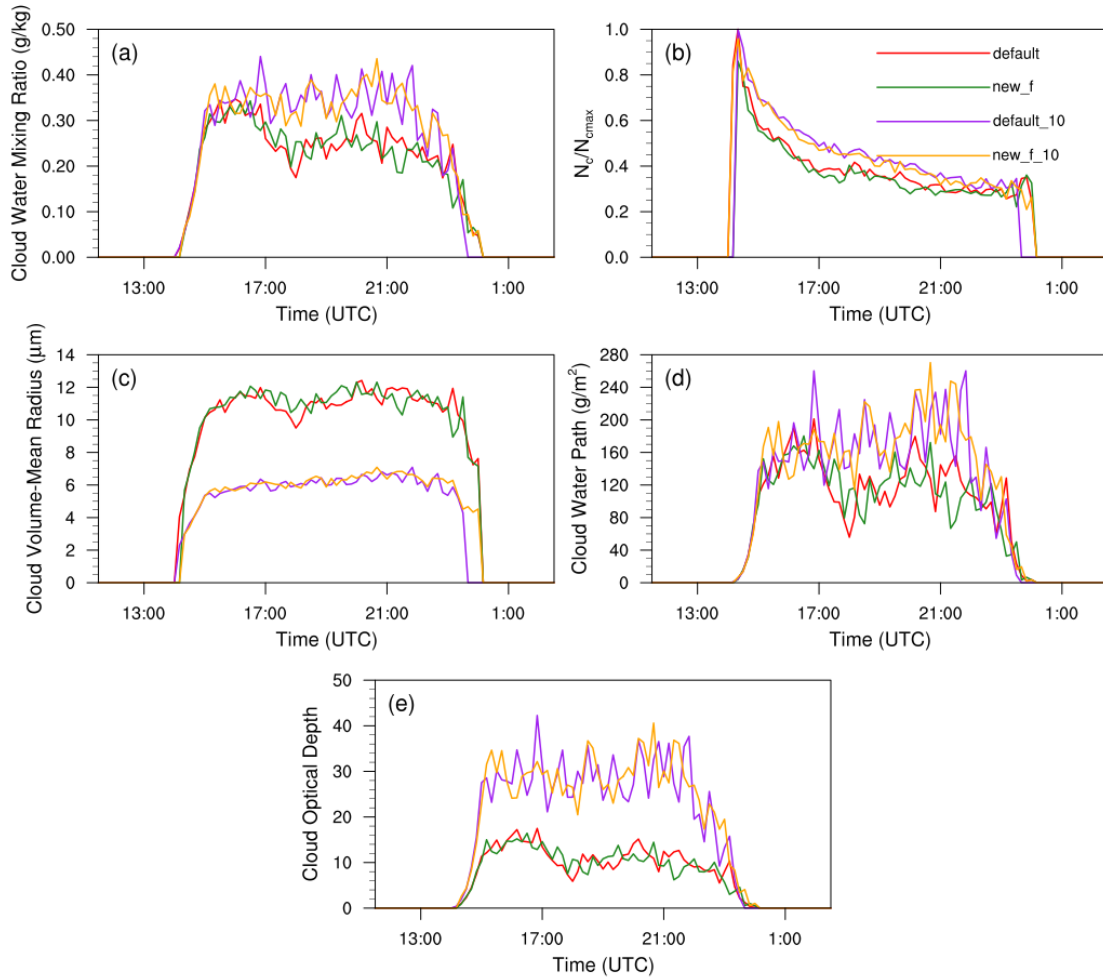
Figure 9. The temporal evolutions of main cloud microphysical and optical properties

in all simulation experiments for the cumulus case, including (a) cloud water mixing

ratio ($q_c$) (g/kg), (b) cloud droplet number concentration ($N_c$) (/cm$^3$), (c) cloud droplet

volume-mean radius ($r_v$) (μm), (d) cloud water path (CWP) (g/m$^2$), and (e) cloud optical

depth ($\tau$). In (b), $N_c$ in the experiments *default* and *new_f* are normalized by the

maximum cloud droplet concentration ($N_{cmax}$) from *default*, respectively; $N_c$ in the

experiments *default_10* and *new_f_10* are normalized by $N_{cmax}$ from *default_10*,

respectively. *new_f* and *new_f_10* are the experiments using entrained air relative

humidity.
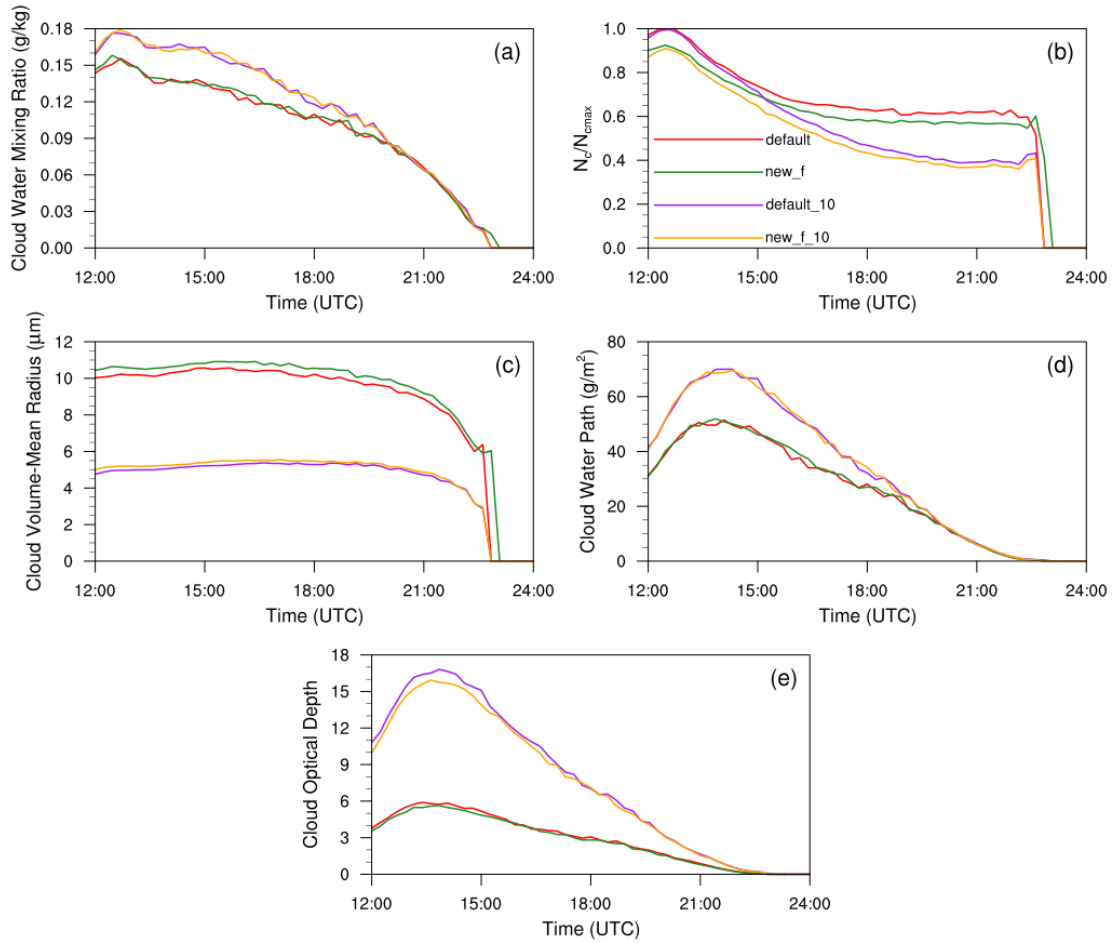
833

834  Figure 10. The temporal evolutions of main cloud microphysical and optical properties

835  in all simulation experiments for the stratocumulus case, including (a) cloud water

836  mixing ratio ($q_c$) (g/kg), (b) cloud droplet number concentration ($N_c$) (/cm$^3$), (c) cloud

837  droplet volume-mean radius ($r_v$) (μm), (d) cloud water path (CWP) (g/m$^2$), and (e) cloud

838  optical depth ($\tau$). In (b), $N_c$ in the experiments *default* and *new* are normalized by the

839  maximum cloud droplet number concentration ($N_{cmax}$) from *default*, respectively; $N_c$ in

840  the experiments *default_10* and *new_10* are normalized by $N_{cmax}$ from *default_10*,

841  respectively. *new_f* and *new_f_10* are the experiments using entrained air relative

842  humidity.

843